ECAP-2018

Alignment of KM3NeT/ORCA - Calibration of the AHRS data and investigation of the sea current

Bachelorarbeit aus der Physik

Vorgelegt von
Benjamin Andreas Schwab
14.08.2018

Erlangen Centre for Astroparticle Physics
Physikalisches Institut IV
Friedrich-Alexander-Universität Erlangen-Nürnberg

1. Gutachter: Dr. Thomas Eberl
2. Gutachter: Prof. Dr. Gisela Anton

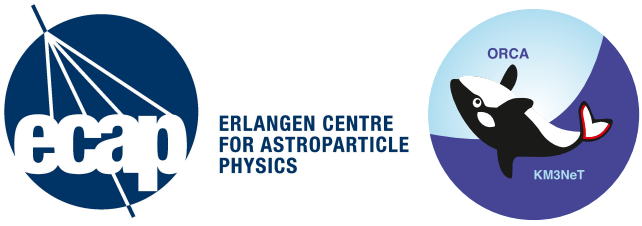

Contents

1 Abstract

To determine the neutrino mass hierarchy, the KM3NeT3/ORCA detector has a 3D array of Digital Optical Modules (DOMs/Cherenkov light detectors) implemented as lines in the Mediterranean sea. These lines deform due to the present sea current. It is therefore the goal to describe the line shape to monitor the position of the DOMs. In order to archive this, the line shape model of the ANTARES detector will be implemented by using the positioning data of each DOM (Tait-Bryan angles). But these are miscalibrated and must therefore be recalibrated. Hence, it is essential to determine the local attributes of the sea current. For this reason, the ADCP (Acoustic Doppler current profiler) detector of the ORCA detector will be verified and used to determine the velocity and direction of the sea current. With the understanding of the sea current it is possible to recalibrate two of the three Tait-Bryan angles, which is sufficient to understand the line shape.

2 Introduction

In 2015, T. Kajita and A. McDonald won the Nobelprize for proving neutrino oscillation via disappearance of atmospheric muon neutrino at the Super-Kamiokande neutrino detector. A atmospheric neutrino flux is produced due to the constant flux of about 1000 $\frac{1}{m^2 s}$ cosmic rays hitting Earth. The first encounter of the primary particle, e. g. a proton or iron nucleus, with a atmospheric atom, e. g. nitrogen, leads to the production of several pions, koans and other nuclei, but mainly pions. These procedures cascade hadronic showers, producing more and more hadrons, especially pions, which then decay into muons and muon antineutrinos. Then again, before they reach the ground, they decay into a muon neutrino, an electron antineutrino and a electron.

$$\begin{aligned} \pi^+ &\rightarrow \mu^+ + \nu_\mu \qquad (1) \\ &\quad \hookrightarrow e^+ + \nu_e + \overline{\nu}_\mu \\ \pi^- &\rightarrow \mu^- + \overline{\nu}_\mu \qquad (2) \\ &\quad \hookrightarrow e^- + \overline{\nu}_e + \nu_\mu \end{aligned}$$

This means that the muon neutrino to electron neutrino ratio should be roughly 2:1. But then Super-Kamiokande and several other detectors measured some ratio anomalies, formly as:

$$R = \frac{(\frac{N_\nu}{N_e})_{\text{obs}}}{(\frac{N_\mu}{N_e})_{\text{theory}}} = 0.60 \quad [8]. \qquad (3)$$

Because the Super-Kamiokande detector is a water Cherenkov detector, it was possible to determine the direction of the neutrinos. T. Kajita and his collaboration then proceed to explain that the neutrino flux of the atmosphere is symmetric, meaning that the neutrino flux at the detector should be equal, whether if it comes from the top atmosphere or the atmosphere at the opposite side of Earth.
While this statement is true for electron neutrinos, a disappearance of muon neutrinos from the opposite side of the Earth is visible. This means that the muon neutrinos oscillated into tau neutrinos while traveling through the Earth. Additionally was a tau appearance measured at 4σ [8]. All in all, this excludes other hypotheses as neutrino decoherence or neutrino decay. For further details see [8].
The flavour oscillation of neutrinos can be modelled by the Pontecorvo-Maki-Nakagawa-Sakata (PMNS) matrix U, which gives the mixing between the mass eigenstates and the flavour eigenstates,

$$\begin{pmatrix} \nu_e \\ \nu_\mu \\ \nu_\tau \end{pmatrix} = \begin{pmatrix} 1 & 0 & 0 \\ 0 & c_{23} & -s_{23} \\ 0 & s_{23} & c_{23} \end{pmatrix} \times \begin{pmatrix} c_{13} & 0 & -s_{13}e^{-i\delta} \\ 0 & 1 & 0 \\ s_{13}e^{-i\delta} & 0 & c_{13} \end{pmatrix} \times \begin{pmatrix} c_{12} & -s_{12} & 0 \\ s_{12} & c_{12} & 0 \\ 0 & 0 & 1 \end{pmatrix} \times \begin{pmatrix} \nu_1 \\ \nu_2 \\ \nu_3 \end{pmatrix} [8], \qquad (4)$$

where $c_{ij} = \cos(\theta_{ij})$, $s_{ij} = \sin(\theta_{ij})$, θ_{ij} is the mixing angle between the mass eigenstates i and j, and $e^{-i\delta}$ is the CP-violating phase. These open parameters θ_{ij} and $e^{-i\delta}$ have to be

determined experimentally, because the PMNS matrix can only describe the phenomena but not explain it.
This leads to several questions. The first one to notice is that the mechanism builds on the fact, that the flavour eigenstates are a linear combination of the mass eigenstates. But according to the standard model of particle physics, neutrinos should be massless. Therefore it is from interest to determine these new open parameters.
Another question is, how the neutrino propagate through spacetime and what the probabilities of measuring a certain flavour are, after such propagation. This can easily be illustrated by the two flavour case:

$$\mathrm{P}_{\mu\to\tau} = |\langle\nu_\tau(t)|\nu_\mu\rangle|^2 = \sin^2(2\theta)\sin^2\left(\frac{\Delta m^2 L}{4E_\nu}\right) \text{[8]}, \tag{5}$$

$\Delta m = m_1^2 - m_2^2$: mass difference of the two eigenstates
L: oscillation baseline
E_ν: neutrino energy

As we see, equation 5 depends on the mass difference of the mass eigenstates. This means that it is possible to determine the mass difference through oscillation measurements, which resolved in $\Delta\mathrm{m}_{12}^2 = 7.54 \cdot 10^{-5}\mathrm{eV}^2$ and $|\Delta\mathrm{M}^2| = 2.43 \cdot 10^{-3}\mathrm{eV}^2$ [10] in the natural unit system. The positive sign of $\Delta\mathrm{m}_{12}^2$ determines that the first mass eigenstate is heavier than the second one. However, $|\Delta\mathrm{M}^2|$ behaves a bit different, because of the unknown sign and whether it is the difference of the third mass state with the first or second one. This characteristics resolves in two different mass hierarchies, the normal and the inverted hierarchy as seen in figure 1.
The oscillation probabilities also changes in matter due to the possibility of additional charged current interactions of electron neutrinos with electrons. This asymmetry of interaction leads to a possible resonance of flavour transition, only depending on the energy and the propagation length in matter. This means that even when the mixing angles and therefore the probabilities of flavour transition are small in vacuum, there is a high chance of flavour transition possible. Important to mention is that this resonance is only possible for neutrinos or anti neutrinos but not for both, depending on the mass hierarchy. For more details see [13].
Due to resonance effects in the oscillation depending on the hierarchy, it is the goal of ORCA to determine the hierarchy. Also to enable such high precision measurements it is important to fully understand the detector and its positioning of the individual detector units and their alignment. Therefore it is also important to understand the dynamics of the deep sea around the ORCA infrastructure.

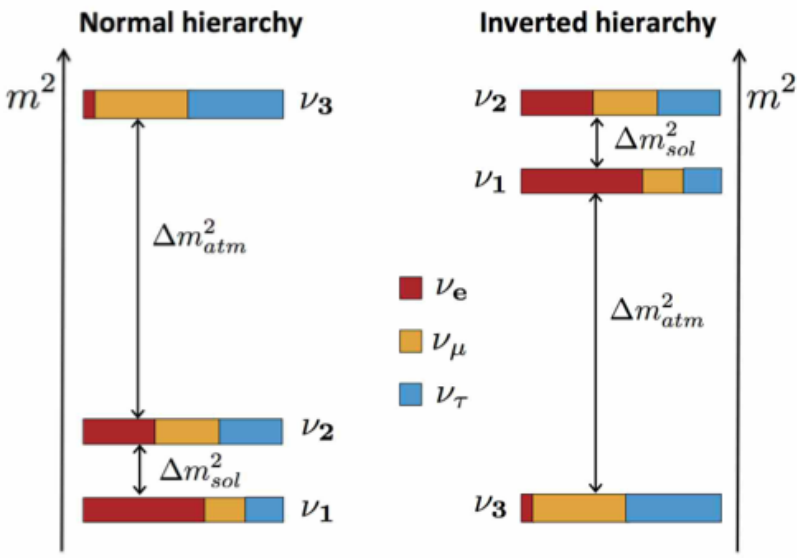

Figure 1: Here are $|\Delta M^2| \equiv \Delta m^2_{atm}$ and $\Delta m^2_{12} \equiv \Delta m^2_{sol}$ to illustrate the two possible neutrino mass hierarchies.

3 KM3NeT/ORCA

3.1 Detection principle

3.1.1 Neutrino interactions

Neutrinos only have a weak charge and can therefore only interact via charged or neutral current, meaning there are only two prime topologies for interaction with water nuclei (see figure 2). Each neutrino interaction with an nuclei leads to a hadronic shower and a secondary particle depending on the interaction. For the charged current is a lepton of the same flavour produced. This leads to three sub topologies: The low radiation length of the electron leads to an additionally electromagnetic shower, the muon leaves a long tracklike signature and the low life time of the tau lepton results in a second hadronic shower. In contrast to the charged current, leads the neutral current to a neutrino of the same flavour. While the secondary produced leptons from the charged currents can be measured directly, it is not possible to measure neutrinos directly. This makes the energy and direction measurement way more difficult.

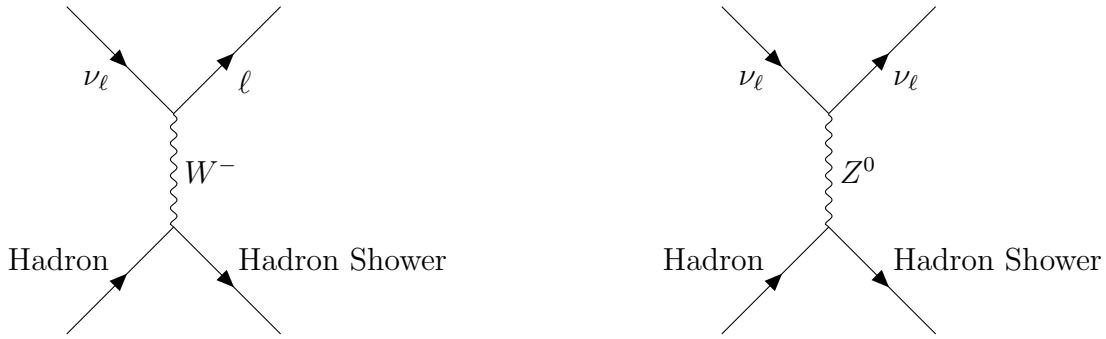

Figure 2: Left: Chaged current interaction; Right: Neutral current interaction; These Feynman diagrams are just for illustration and not fully mathematically correct.

3.1.2 Cherenkov light signature

Charged particles, like in neutrino interaction produced leptons, with superluminal speed in a medium emit Cherenkov radiation. This is due to the effect, that charged particles propagate through matter induce dipoles, which then emit radiation. Normally this radiation interferes destructive, leading to no emission of light in the macroscopic picture. But when the particle that is inducing the dipoles in the medium propagates faster than the speed of light, the emitted radiation of the prior source can not interfere destructive with the next source, leading to a macroscopic emission of light.
Epitomised through the Huygens principle, where each source emits a spherical wave (picture 3), a wavefront is created behind the particle in the form of a cone with an

opening angle depending on the refractive index n of the medium and its relativistic speed $\beta = \frac{\mathrm{v}}{\mathrm{c}}$:

$$\cos(\theta) = \frac{1}{\mathrm{n}\beta} \quad . \tag{6}$$

This wavefront can also be interpreted as shockwave of photons, which also leads to the characteristic enlighten circles in the detector. For water the opening angle of the cone is about 42°.

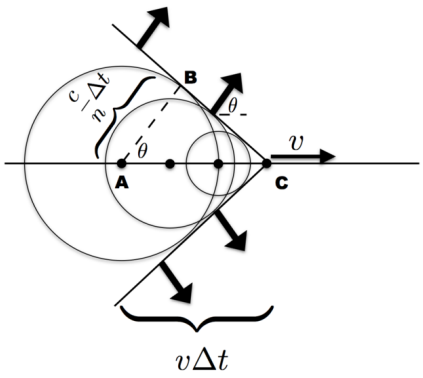

Figure 3: Huygens principle of spherical wavelets [4].

3.1.3 Analysis of the events

The Cherenkov light from the showers and leptons of the neutrino interactions can then be measured by the 3D array of ORCA. By the amount of Cherenkov photons and the geometry of the cone can the energy and the direction of the neutrino be determined. To investigate which hierarchy is realised in nature, it must be able to distinguish between neutrinos and antineutrinos. Because ORCA measures only the emitted Cherenkov light, it is not possible to directly distinguish between them.
Therefore a statistical separation is used, which relies on the fact, that neutrinos and anti neutrino have a different cross section in the energy range of atmospheric neutrinos. The cross section of anti neutrinos is about $\frac{1}{2}$ lower than that of a neutrinos depending on the energy. Consequently, if there are more electron and muon neutrinos measured that are convenient to the resonance mechanism, the normal mass hierarchy is verified, because neutrinos have a larger cross section. For detailed information see [2].

3.2 ORCA detector structure

The ORCA detector is build about 40km offshore from Toulon, France, at the bottom of the Mediterranean Sea in a depth of 2450m and about 10km east of the ANTARES detector. In precise coordinates: 42° 48' N 06° 02' E.
The detector has a instrumented volume of 8Mm^3 of water as detection material in a cylindric form with a radius of about 120m and a height of about 197m.

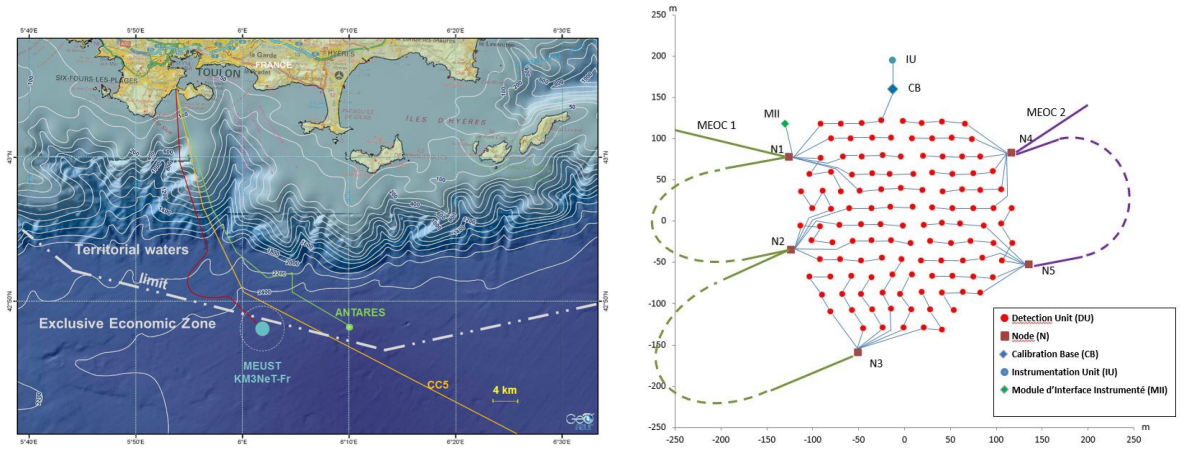

Figure 4: Left: Location of ORCA as KM3NeT-Fr and ANTARES [2]; Right: Footprint of ORCA [7].

The instrumentation of the volume of about 8Mt of water is accomplished by 115 detection units (DU), which are strings of about 197m length with 18 digital optic model (DOMs) and a top buoy for the needed uplift. From a height of 40m above the sea ground, the DOMs are equally distributed in a distance of 9m. The horizontal spacing between the DUs is about 23m. These informations are out of the letter of intent [2] and had been actualised.

3.2.1 DU structure

The DUs of ORCA are composed of two parallel Dyneema ropes with a diameter of 4mm. Above 40m of the sea bed is every 9m a DOM fixed with a titanium collar. Additionally spacers are added to keep the ropes parallel and to minimize the torque.
Due to the spherical symmetry it is not important how the DU is orientated. Therefore it gets fixed with a random orientation into the sea bed. To minimize the deformation of the line shape, an additionally buoy is placed at the top of the DU, although the buoyancy of the DOMs and cables would be sufficient. A sketch of a DU can be seen in figure 5.

Figure 5: Left: Structure of a DU; Right: Close-up view of a DOM [2]

3.2.2 DOM structure and the AHRS data

A DOM consists of a 17 inch diameter glass sphere with 31 PMTs (Photo-multiplier tubes) (as seen in figure 5) and the readout electronics. Onto the central logic board of the readout electronics, a AHRS (attitude and heading reference system) board is installed. It is taking the data of the three Tait-Bryan angles[1] yaw, pitch and roll, the acceleration and angular acceleration in each spatial direction, and the magnetic field projection in each spatial direction.
For the alignment of ORCA, only the yaw, pitch and roll angles and the magnetic field projections are relevant. But the magnetic field projection data is not available for the time period in which ORCA was operating (see chapter 3.3). Therefore the alignment must be recreated with only the Tait-Bryan angles, which is still possible.

3.2.3 Tait-Bryan angles

There are different ways to describe the rotation of a body in three dimensions. One of them are the Tait-Bryan angles, which are three rotation angles around three different axis, which are also standard in the aerospace industry. Each angle around a specific axis has his own name: yaw for the rotation around the z axis, pitch for the y axis and roll for the x axis. For the application on the AHRS board see figure 6. To cover all

[1] similar to Euler angles

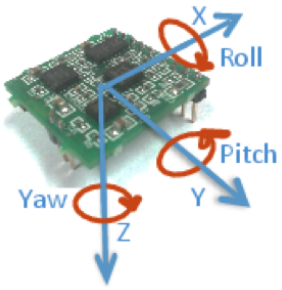

Figure 6: The AHRS board and its coordinate system [3].

possible positions must span the yaw and roll angle from $[-\pi, -\pi]$ and the pitch angle from $[-\frac{\pi}{2}, \frac{\pi}{2}]$.
These rotation can be described by rotation matrices. But this also means that for three rotation are six orders of rotations possible, because these type of matrices are not commutative. A simpler approach would be that every rotation also let the coordinate system rotate, meaning that the axis are not fixed in space. The rotation order is therefore standardised to yaw-pitch-roll [11]. The associated matrix can be seen in the following equation:

$$R_{ij} = \begin{pmatrix} c(y) & -s(y) & 0 \\ s(y) & c(y) & 0 \\ 0 & 0 & 1 \end{pmatrix} \times \begin{pmatrix} c(p) & 0 & -s(p) \\ 0 & 1 & 0 \\ s(p) & 0 & c(p) \end{pmatrix} \times \begin{pmatrix} 1 & 0 & 0 \\ 0 & c(r) & -s(r) \\ 0 & s(r) & c(r) \end{pmatrix} \tag{7}$$

$$= \begin{pmatrix} c(p)c(y) & -s(r)s(p)c(y) - c(r)s(y) & c(r)s(p)s(y) + s(r)s(y) \\ c(p)s(y) & s(r)s(p)s(y) + c(r)c(y) & c(r)s(p)s(y) - s(r)c(y) \\ -s(p) & s(r)c(p) & c(r)c(p) \end{pmatrix} . \tag{8}$$

Again are the c(...) and s(...) terms cos(...) and sin(...), while y, p and r, stands for yaw, pitch and roll. With a standardised vector as $(0, 0, 1)^T$ for example, it is possible to reconstruct the positioning of the given DOM.

3.3 Current state

ORCA is still in the construction phase. The first from 115 DUs was deployed in September 2017. Since then took the DU data until the main electro-optical cable had a failure in mid December and made it impossible to operate the detector [12]. Therefore all the available data is from the first deployed DU and the stated time span.
For the future of the detector will be a new electro-optical cable and the remaining DUs deployed. The expected year for the completion of the detector is 2020 [2].

4 ANTARES line shape model

The previously mentioned ANTARES detector is the prototype of all KM3NeT detectors. Therefore is the concept of the detectors very similar. The main differences are the spacing between the DUs and the DOMS, the height of the DUs and the DOMs themself. Instead of the glass sphere with 31 80mm PMTs and the whole electronic inside, ANTARES storeys with three 10" PMTs are used, which look downward in an angle of 45°.
Due to the present sea current the line shape is deformed, leading to an unknown position of the storeys. In order to determine their position, a mechanical model was developed. This section will be a summary of the line shape model of ANTARES described in the following paper [1].
At every point of the line, especially at the storeys, a vertical force W due to its buoyancy and a horizontal force F as a result of the flow resistance (equation 9) can be assigned:

$$F = \frac{1}{2} c_w A \rho v^2 \ . \tag{9}$$

The drag coefficient c_w and the cross section A are individual parameters of the components, ρ is the pressure of the water and v the velocity of the sea current. By measuring the buoyancy, drag coefficient and cross section of each component, it is possible to characterise the active forces on each component.
Summing now all forces above point i allows it to give the respective slope of given point i as the ratio of the horizontal and vertical forces:

$$\frac{\mathrm{dr}}{\mathrm{dz}} = \frac{\sum_{j>i}^{N} F_i}{\sum_{j>i}^{N} W_i} \ . \tag{10}$$

To simplify the model it is assumed that the mass of each component is distributed equally on the line. Then it is possible to write the forces down as:

$$W(z) = [\mathrm{n}(W_{\text{storey}} + W_{\text{12m cable}}) + W_{\text{100m cable}}] \frac{h-z}{h} + W_{\text{buoy}} \quad , \tag{11}$$

$$F(z) = [\mathrm{n}(F_{\text{storey}} + F_{\text{12m cable}}) + F_{\text{100m cable}}] \frac{h-z}{h} v^2 + F_{\text{buoy}} v^2 \quad , \tag{12}$$

where n is the number of storeys, which is 25 for ANTARES. W_{storey}, F_{storey} and $W_{12\text{ m cable}}$, $F_{12\text{ m cable}}$ are the forces on the storeys and the 12 meter cable between them, therefore are n such force terms into the equation. Because there are 100 meter from the sea bed to the first storey an additionally term must be added in form of $W_{100\text{m cable}}$ and $F_{100\text{m cable}}$. On top of that comes the top buoy with W_{buoy} and F_{buoy}. The $\frac{h-z}{h}$ term assures that all points below z are neglected for each point at height z.
Due to this simplification it is possible to write equation 10 down as:

$$\frac{\mathrm{dr}}{\mathrm{dz}} = \frac{F(z)}{W(z)} = \frac{a - bz}{c - dz} v^2 = g(z) \ , \tag{13}$$

with

$$a = 25(F_{\text{storey}} + F_{\text{12m cable}}) + F_{\text{100m cable}} + F_{\text{buoy}} \ , \tag{14}$$

$$b = \frac{25}{h}(F_{\text{storey}}) + \frac{1}{h}F_{\text{100m cable}} \ , \tag{15}$$

$$c = 25(W_{\text{storey}} + W_{\text{12m cable}}) + W_{\text{100m cable}} + W_{\text{buoy}} \ , \tag{16}$$

$$d = \frac{25}{h}(W_{\text{storey}}) + \frac{1}{h}W_{\text{100m cable}} \ . \tag{17}$$

By an integration of equation 10 the given line shape is:

$$r(z) = \left[\frac{b}{d} - \frac{ad - bc}{d^2}\ln\left(1 - \frac{d}{c}\cdot z\right)\right]v^2 \ . \tag{18}$$

4.1 Applying the line shape model to ORCA

Because of the comparable structure of ANTARES and ORCA it is possible to apply the line shape model of ANTARES to the ORCA geometry. Of course there must be several adjustments due to the specifications of each detector. The first one is that the ropes and the DOMs have a different buoyancies and flow resistances, because of the different designs. Instead of the thick rope and three PMTs in each storey of ANTARES, two slimmer Dyneema ropes and a spherical DOM design are used for ORCA. Therefore all force parameters W and F must be replaced by ORCA specific parameters.
The second one is that ORCA only has 18 DOMs in a distance of 9m, which start 40m above the seabed to a high of h = 197m. All in all, are now the equations given as,

$$W(z) = 18(W_{\text{DOM}} + W_{\text{9m cable}})\frac{h - z}{h} + W_{\text{40m cable}} + W_{\text{buoy}} \ , \tag{19}$$

$$F(z) = 18(F_{\text{DOM}} + F_{\text{9m cable}})\frac{h - z}{h}v^2 + F_{\text{40m cable}} + F_{\text{buoy}}v^2 \ , \tag{20}$$

with parameters from the collaboration meeting in Granada (08.05.2018):

Table 1: Force parameters for each component of ORCA [5].

	DOM	9m cable	40m cable	buoy
W $[\frac{\text{Ns}^2}{\text{m}^2}]$	130	0	0	1050
F [N]	38.5	13.9	61.8	42.6

Leading to new a,b,c,d coefficients in equation 13 and 18:

$$\text{a} = 1005 \text{ N}, \quad \text{b} = 5.1 \text{ N}, \quad \text{c} = 3390 \ \tfrac{\text{Ns}^2}{\text{m}^2}, \quad \text{d} = 11.9 \ \tfrac{\text{Ns}^2}{\text{m}^2} \ .$$

4.2 Translation of the AHRS data to the line shape model

The ANTARES model is able to determine the line shape with a given velocity v, but in general the velocity of the sea current is unknown. Therefore it is the task to determine the alignment through the AHRS data and then calculating the velocity from the given line shape.
The first step is to take the standardised positioning vector $(0,0,1)^T$ of a DOM, when the DU is completely straight and rotate it into position with the in chapter 3.2.3 introduced rotation matrix. The given angles are measured via the AHRS board in the DOMs. With the inverted slope of the positioning vector will then the velocity of the sea current be calculated as seen in equation 13. The correlation can be seen in figure 7.

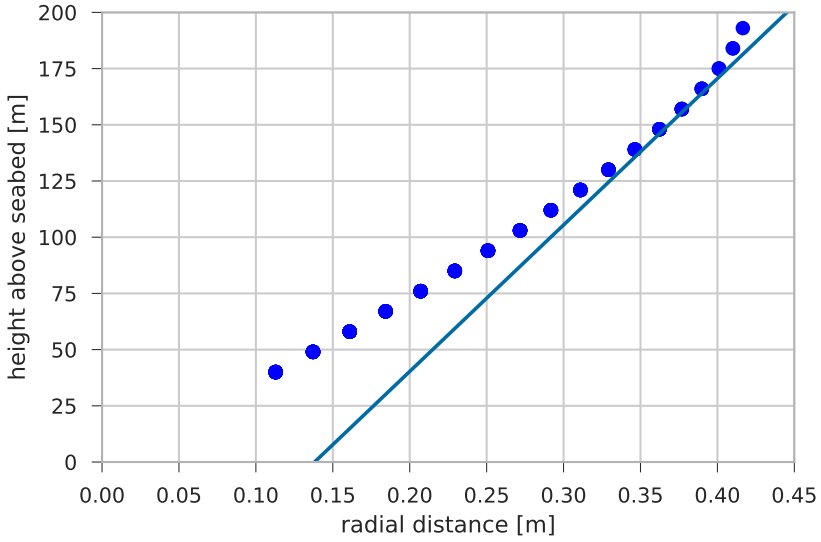

Figure 7: The slope of the positioning vector equates the slope of the line shape at the position of the DOM.

Then it is able to determine the radial distance of the DOM with equation 18 for the DOM at given height $z = 40\text{m}+9 \cdot (\text{floor} - 1)\text{m}$. This equation assumes that the line is straight, which is obviously not the case. But even at the highest sea currents ($v \approx 30\frac{\text{cm}}{\text{s}}$) is the maximum discrepancy between the real, height and the simplistic one 4cm. For the common speeds of 10 $\frac{\text{cm}}{\text{s}}$ it is even below 0.06cm, which validates the assumption.
With this method it is now possible to determine the positioning of each DOM in a 2D frame. Of course could the vectors be all rotated a bit differently around the yaw angle, but the DU is very stiff and very resistant to torque. Therefore it is neglectable.
Through these points will the line shape be fitted (equation 18) with the velocity of the sea current as the free to determine parameter. A idealised example is seen in figure 8.
With the now given algorithm it is possible to determine not only the line shape but also the sea current velocity.

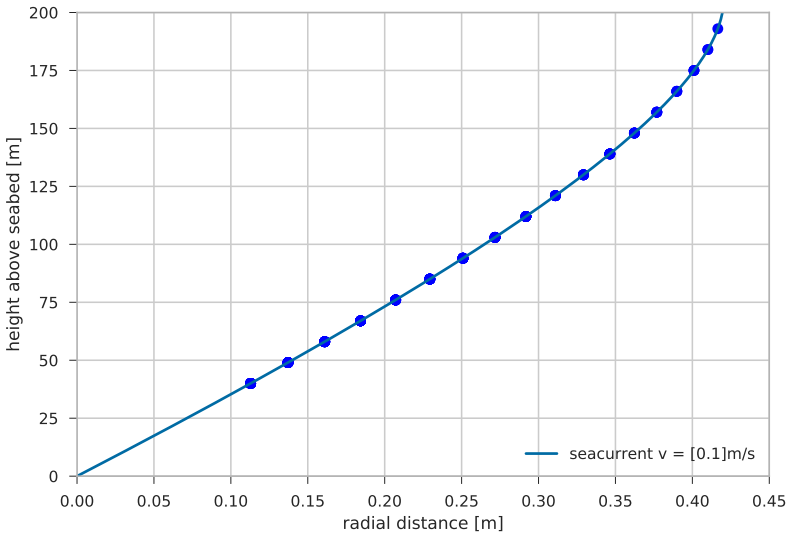

Figure 8: Theoretical fit through perfectly aligned DOMs for a sea current velocity $v = 10\frac{\text{cm}}{\text{s}}$.

5 Data analysis

5.1 AHRS data

The first task to reconstruct the alignment and the sea current is to check the AHRS data if these are precise enough. The question is not about the resolution, but about a possible absolute offset of a few degrees. Such offset would have a major influence as following toy calculation attests:
Assume that the DU is a straight line with height h 197m (linear approximation) and the sea current velocity is at the maximum of $v = 30\frac{\text{cm}}{\text{s}}$. This means that the deflection is also at maximum, which is about 4m. Now calculate the deflection angle φ of the DU:

$$\varphi = \arcsin(\frac{4\text{m}}{197\text{m}}) = 1.16^\circ \ . \tag{21}$$

An offset of a few degrees would therefore make the reconstruction of the line shape impossible without recalibration.
To see if the angles are affected by such offset, they are plotted over a time interval of a few days (figure 9). Because of the changing sea currents should they vary around their true zero value.

Due to reasons of readability of the plots, only the data of the first six DOMs are plotted. In the case of the yaw plot only DOM 2 to DOM5 were plotted, because more data would make the plot unreadable. Adding constants to the data functions to locally separate them would make a analysis of the offset meaningless. The rest of the DOMs are in the appendix (see appendix A).
The first thing to notice is that roll and yaw are not around 0°. The 0° angle of the yaw is so calibrated that it points towards north. Due to the random anchoring of the DU the yaw points in the 235° direction, while the roll of 180° just means that the AHRS board and the DOM are build in flipped.
The second thing is that the angle data seems to correspond well to the sea current as a clear peak at 03.13.18 is visible. It will emerge later that there is actual a rise of the sea current (see figure 11). Also is a fluctuation of the angles visible corresponding to ebb and flood. This indicates that the AHRS board records correctly.
The third thing is that the order of the angle magnitudes of each DOM is not in order. The line shape or curve of the DU is strictly monotonically increasing. Because of the linear form at the bottom should the deflection angles of the lower DOMs almost be identical and then strictly monotonically decrease as the line bends. But this is not the case in the measurements meaning that the angles have a high offset.
The offset of each angle is also clearly visibly when the AHRS data gets implemented into the line shape model as seen in figure 10. The estimated sea current velocity of $58\frac{\text{cm}}{\text{s}}$ is more than unrealistic. Therefore the AHRS must be calibrated to enable a correct calculation of the sea current and the line shape. It also seems that especially the top 3 DOMs are highly miss calibrated.

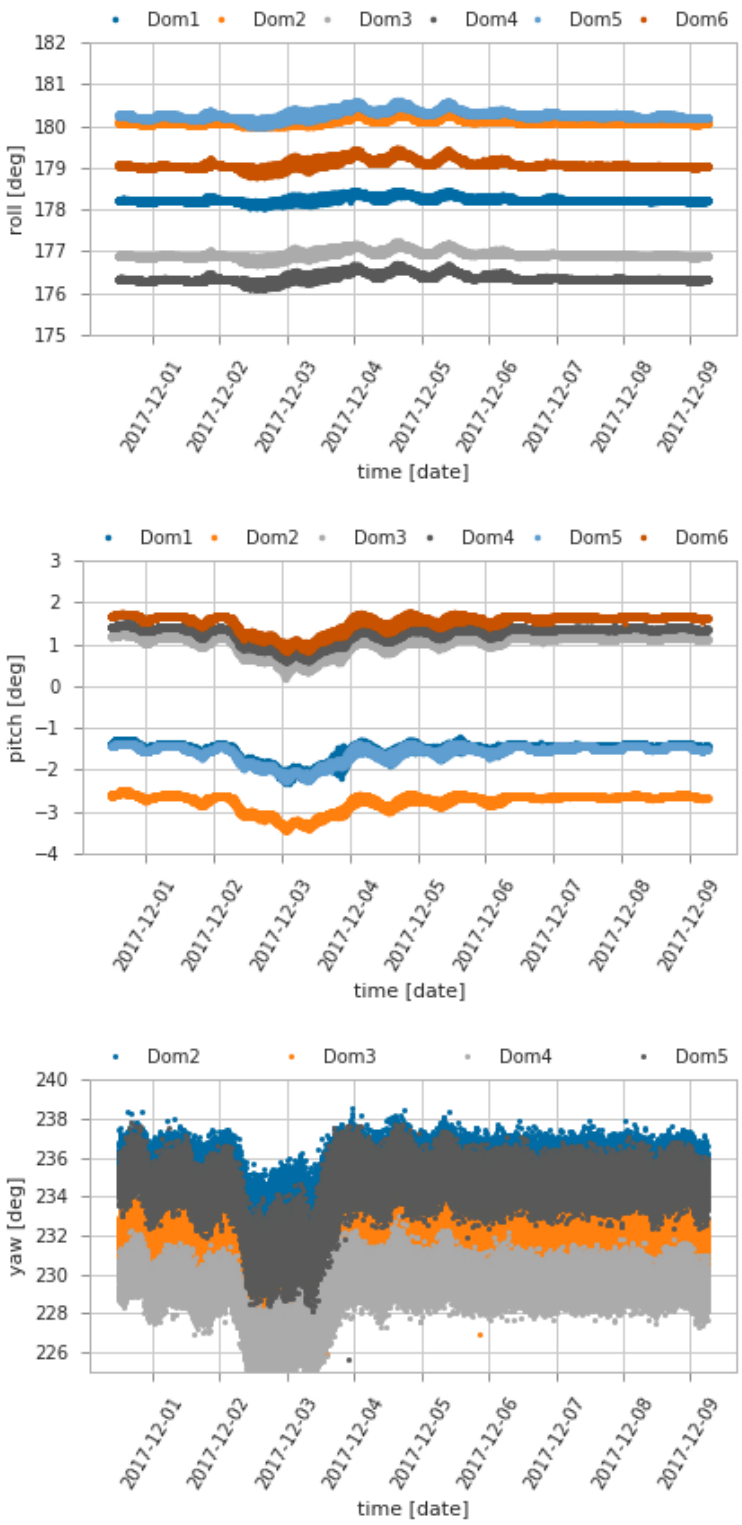

Figure 9: All three Tait-Bryan angles as a time series.

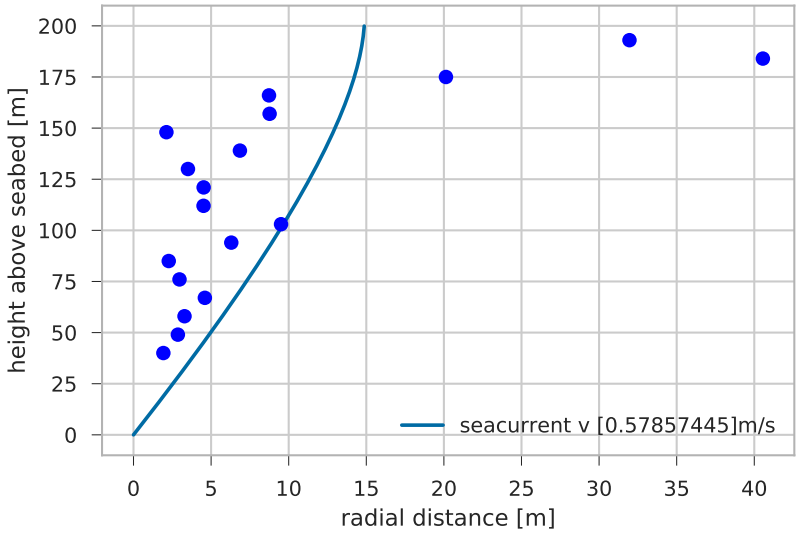

Figure 10: Line shape fit with the raw AHRS data.

5.2 ADCP detector

For the calibration of the DOMs it is essential to have reference data. At the ORCA infrastructure is already a ADCP detector (acoustic Doppler current profiler) of the oceangraphy of Toulon installed, which determines the absolute velocity and direction of the local sea current.
The ADCP sends out sound waves of stipulated frequency, which then get reflected by particles in the current [14]. Flows the current towards the ADCP, gets the prime sound wave Doppler shifted to a higher frequency and vice versa. Hence correlates the Doppler shift with the velocity of the current. The direction of the sea current can then be determined by sending out sound waves in every spatial direction and finding the lowest highest Doppler shift.
The ADCP used is the Aquadopp from Nortek and has a accuracy of $\pm 0.5 \frac{\text{cm}}{\text{s}}$ to the manufacturer specifications [9].

5.3 Verification of the ADCP data

To use the Aquadopp as reference data it must be guarantied that it measures correctly. Additionally, ina distance of 10 km distance, ANTARES is placed with its well understood algorithm to calculate the direction and velocity. The task is therefore to verify the ADCP data. The available data of the two detectors spans from 01.10.17 to 04.12.17 and are taken in 10 minutes intervals for the ADCP [6] and 2 minutes for ANTARES [7]. As can be seen in figure 11, the absolute velocity and direction of both detectors can differ. But that is expected, because both detectors are locally separated, meaning that the local values differ due to local characteristics of the sea. An important concern is the causality of the measurements, when the current is streaming from one detector to

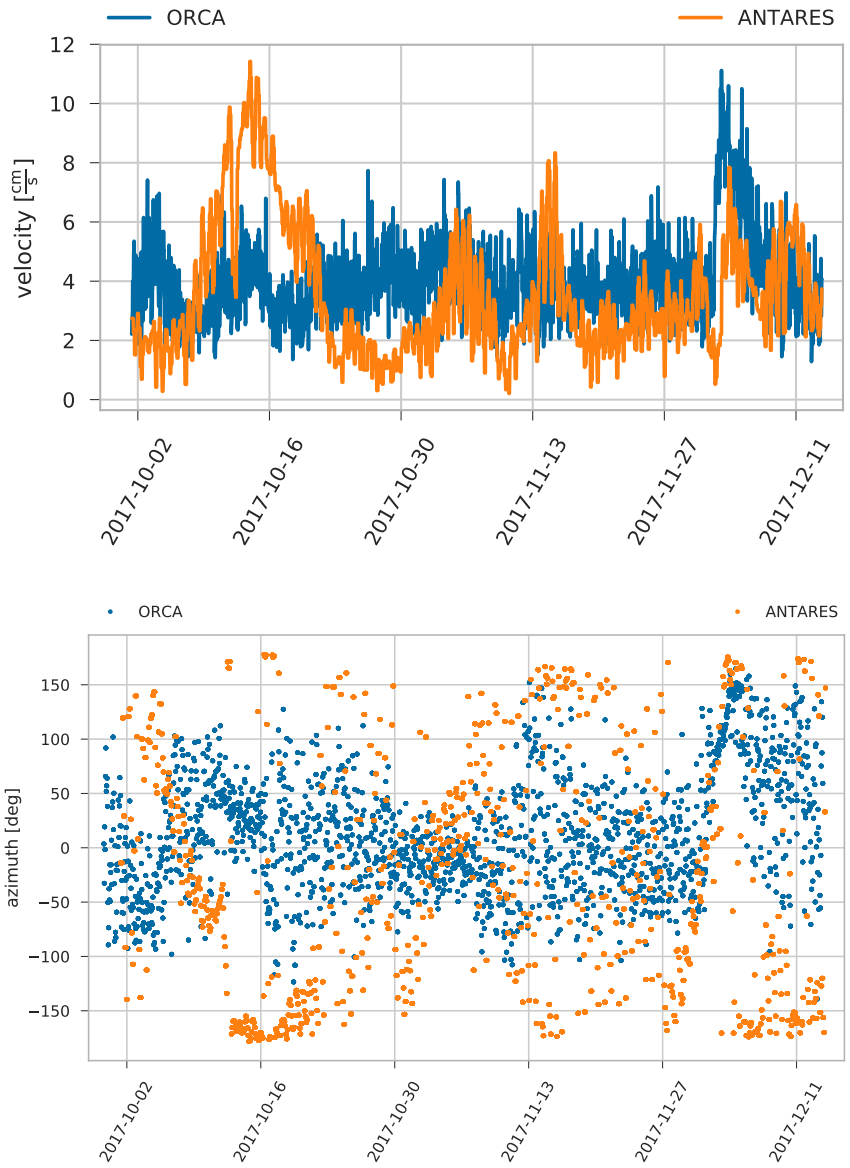

Figure 11: Velocity and direction data of ANTARES and the ADCP at the ORCA site over the whole available time span.

the other. This means, that when the sea current at one detector rises, the other one has to rise too. Of course, this must be depended of the direction and the velocity of the sea current. Is the direction of the sea current from east to west, the rise at ANTARES must be later. How long it takes then to see the velocity increasing at ORCA depends on the absolute velocity of the current.
But it is also possible (as described in the following chapter 5.3.1), that for a certain time interval, the two detectors are in different streaming whirls, meaning that neither the direction nor the velocity of the detectors will correlate.

Also it is clearly visible that the ANTARES direction data is kind of random distributed for velocities below $5\frac{\text{cm}}{\text{s}}$ making a systematically comparison difficult in such time period. Then again are two velocity peaks measured by both detectors, where the direction of the current rotates by 180°. For ANTARES even more. But then again are directions over ± 90° in the v $< 5\frac{\text{cm}}{\text{s}}$ interval and can therefore not be trusted.

5.3.1 Interpretation of the sea currents

A first interpretation of the sea current between the detector shall facilitate the ability of legitimising the ADCP detector.

- **30.09.17-21.10.17 and 11.11.17-09.11.17 and 28.11.17-03.12.17:**
  It is apparent that at every velocity peak of ANTARES the direction turns and then stays at its level for a while. The current at ORCA somehow behaves different. At the first big ANTARES peak is also a peak at ORCA, but the sea current turns in different directions at the detectors. This indicates that both detectors are perchance in two different streaming whirls, which could be due to the current colliding with the continental shelf.
  The second one only occurs at ANTARES. Because of the way it turns, from a direction pointing to west to one pointing to east, can be said that the current accelerates towards ANTARES and vice versa. But only for relative low currents. For the last peak turns the direction of the sea current at both detectors in the same way. Therefore is a linear sea current between the detectors switching from a west direction to an east one.

- **22.10.17-31.10.17 and 10.11.17 27.11.17 and 04.12.17-14.12.17:**
  In these time intervals are the velocities $5\frac{\text{cm}}{\text{s}}$, making the determination of sea current direction difficult. For ANTARES it is even randomly distributed. A statement about the sea current is therefore not significant. But all in all can be said that sea is pretty still.

5.3.2 Correlation between the sea currents

To verify mathematically if the ADCP detector is suitable for the calibration of the DOMs, a cross correlation between the ADCP and the ANTARES measurements is made. Because of the 10 kilometer distance between the detector, a certain lag time can be visible, depending on the speed of the current to reach ORCA. Therefore will be the cross correlation plotted as function over different lag times, as seen in the following equation,

$$C = \frac{\langle (v_{\mathrm{ANTARES}}(t+\tau) - \mu_{\mathrm{ANTARES}}) \cdot (v_{\mathrm{ADCP}}(t) - \mu_{\mathrm{ADCP}}) \rangle_t}{\sigma_{\mathrm{ANTARES}} \cdot \sigma_{\mathrm{ADCP}}} \ , \tag{22}$$

where the angle brackets are a temporal average function of a certain time interval, defined as:

$$\langle f(t) \rangle_t := \frac{1}{N} \sum_{n=1}^{N} f(t_n) \ . \tag{23}$$

Because the given data is in form of a time series, t_n is n times the time between the measurements and N the number of all time steps. Furthermore is μ the mean of the sea current of that time interval and σ the corresponding standard deviation.
The lag time is therefore defined as the time interval the current needs to get from the ANTARES detector to the ADCP and can be in consequence of this definition negative if the current flows in the opposite direction. Also through the steadily changing of the velocity and direction of the sea current, the lag time will change over time. For example, if the direction of the sea current changes from an east direction to a west direction, the lag time will change sign, because of the causality where the stream appears first. Therefore the cross correlation can not be calculated over the whole time period but over smaller time intervals, which are small enough to react to such changes. This leads to the sliding window technique.

5.4 Sliding window technique

This technique takes the measurements of the ORCA detector in a time interval of length T, starting at the point in time P and compares it with the measurement of the ANTARES detector in a time interval with the same length T. But unlike the ORCA interval, which is fixed, the ANTARES interval can be shifted around the time P to compensate the unknown lag time τ.
To roughly estimate the maximum lag time and therefore shift, a toy calculation like the following is made:

$$\tau_{max} \approx \frac{10\mathrm{km}}{v_{\mathrm{min}}} \ . \tag{24}$$

For a minimal velocity of $2.8\frac{\text{cm}}{\text{s}}$, the maximum lag time τ_{max} is about 100 hours. Lower velocities can be ignored because the detectors, or atleast ANTARES, are not able to resolve such small velocities. Therefore are higher lag times not required.
Now the correlation for the time interval T can be calculated for each possible lag time $-\tau_{max} < \tau \leq \tau_{max}$ and graphically plotted as a C-τ-diagram. After these calculations the interval or window will be shifted in time by d. This procedure will then be iterated until the complete time interval is covered.
Important to mention are effects at the edge of the complete data frame, which must be taken into account to ensure that the correlation plot of each window is comparable. If the selected window is completely at the edge of the data frame and the ANTARES time interval gets shifted out of the data frame, the amount of comparable measurements gets smaller because the ANTARES data has no ORCA counterpart outside the data frame. Therefore the window gets smaller and can not be compared with the other ones, because the mean values changes and therefore the correlation changes with the window size.
To fully circumvent this problem and to get fully comparable plots from the range $-\tau_{max} < \tau \leq \tau_{max}$, the edges of the data frame are avoided.

For the analysis through the sliding window technique, the following parameters are chosen: time interval length T = 5 days and shift parameter d = 1 day. Two prime examples shall now be discussed in detail, one from 22.11.17 to 26.11.17 and one from 11.30.17 to 04.12.17, where the velocity of the current significantly increases.
In the time interval from 22.11.17, the velocity of the current was fairly low ($v \lesssim 5\frac{\text{cm}}{\text{s}}$). In this velocity range, the measurements are contingent to statistical noise and have a higher variance. Consequently means that the measurements independently and randomly fluctuate around their true values (see figure 12). This behaviour leads to lower correlation coefficients as the correlation between two independent random signal fluctuates around zero as can be seen in figure 13.
Another effect clearly visible in the plots are tidal effects. The period of ebb and flood is about T $\approx$ 12,5 hours, which is half the time the moon needs to stand above the same point above the Earth after an Earth rotation. But it also depends on the local attributes of the sea and can therefore be longer or shorter. Due to the small distance between ANTARES and ORCA on a global scaling, tidal effects occur at the same time for both detectors. Thus comes a periodic fluctuation on top of the sea current velocity with the addressed periodicity, which is independent of the intrinsic current. This fluctuation is therefore independent of the lag time.
If now the correlation of the tidal effect is calculated with a lag time of $\frac{\text{T}}{2} + \text{T} \cdot \text{n}$ with n $\in \mathbb{N}$ the correlation of ebb and flood will be maximally anti correlated, while with a lag time of T $\cdot$ n with n $\in \mathbb{N}$ it will be maximally correlated.

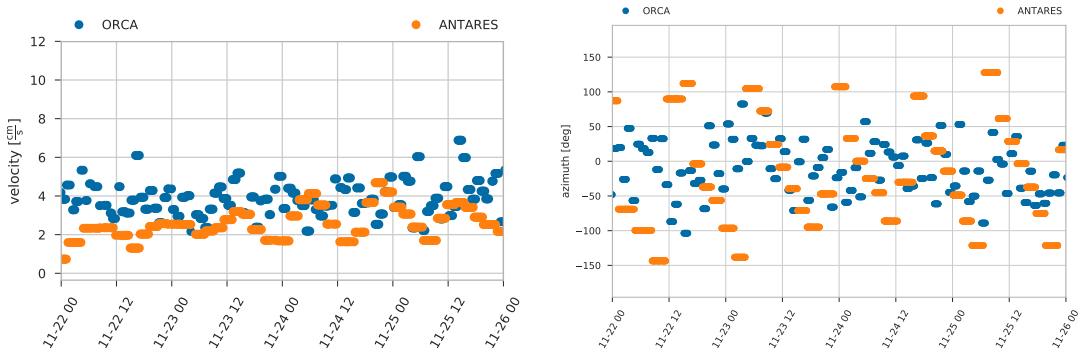

Figure 12: Velocity and direction fluctuations.

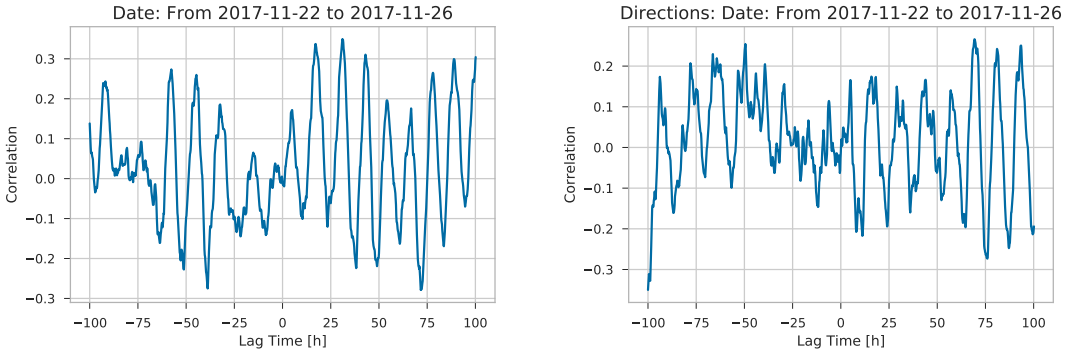

Figure 13: Correlation as a function of lag time.

Therefore is on the top of the correlation function of the sea current a correlation function of the tidal effects with a sinus shape of lower amplitude. For the time interval in figure 13, the velocities are so small that the tidal effects are the dominating effect. Because of the high variances of each measurement and the strong influence of tidal effects in such time intervals means that the data accuracy of both, ANTARES and ADCP, are not trust worthy. For future line shape recreations can therefore the sea current approximated as $0\frac{\text{cm}}{\text{s}}$ due to the low maximum line deflection of 6cm (calculated with $4\frac{\text{cm}}{\text{s}}$). This means that both detectors measure a different random signal around $0\frac{\text{cm}}{\text{s}}$ resulting in low correlation coefficients. But because both detectors measure random signals means implicates a logical correlation, which can not be described by the defined correlation coefficient (equation 22).

In the second time interval from 30.11.17, a clear rise of the sea current and a 180° rotation of the direction is visible (figure 11 down). Because of the high velocities measured is the signal to noise ratio for velocities better in such time intervals (see figure 14). Also is the direction measurement more precise, because the stream is more stable. As seen in figure 15 the correlations are significantly high (above 0.8) and tidal effects have nearly no influence on the correlation function of the velocities. On the direction they are still visible but in a acceptable manner.

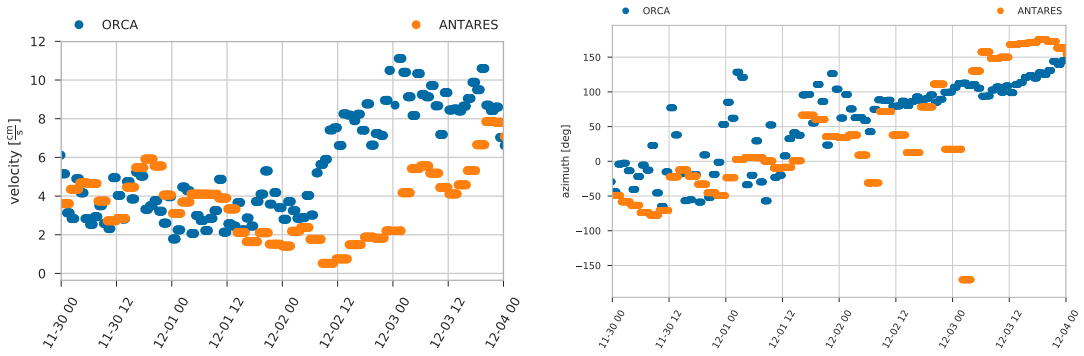

Figure 14: Velocity and direction fluctuations.

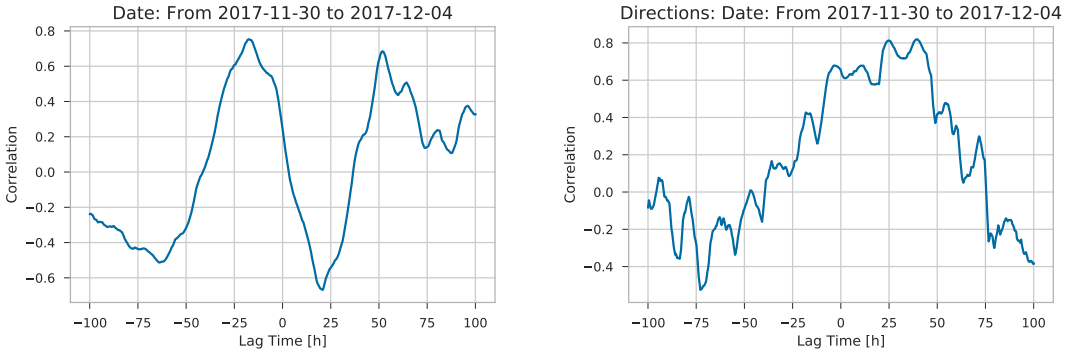

Figure 15: Correlation as a function of lag time.

5.5 Calibration of the DOMs

5.5.1 Setting up the calibration

To set up the calibration for each DOM, a time interval must be chosen in which the sea current of the ADCP is small, or to be precise, $0\frac{\text{cm}}{\text{s}}$. Due to the neglectable sea current, the line shape must then be straight with no deflections. It is then possible to determine the offsets of the pitch and roll angles, because the miss calibrated DOMs will then measure their offsets. For the reason that the yaw angle only rotates the line around its rotational symmetry axis, it does not contribute to the slope of the line and therefore its offset is not from relevance for the determination of the velocity of the sea current.
Of course, the angles could be calibrated in a time interval with high sea currents by creating a calibration positioning vectors of each DOM from the ADCP data and then adjusting the angles to match them. But these methods are vulnerable to errors and could not be realised. Therefore the ADCP data will primarily be used to determine the right time interval for the calibration.

5.5.2 Calibration

The time interval from 18.11.17 to 22.11.17 seems to be optimal as the velocity of the sea current is the lowest of all the available time intervals. Every acquisition of pitch and roll in the chosen time interval will be taken into account and subtracted from the true values of pitch and roll for a complete straight line. For pitch that would be 0° and for roll 180°. The results for two prime examples are displayed in figures 16 and 17. The rest of the plots are in appendix B.

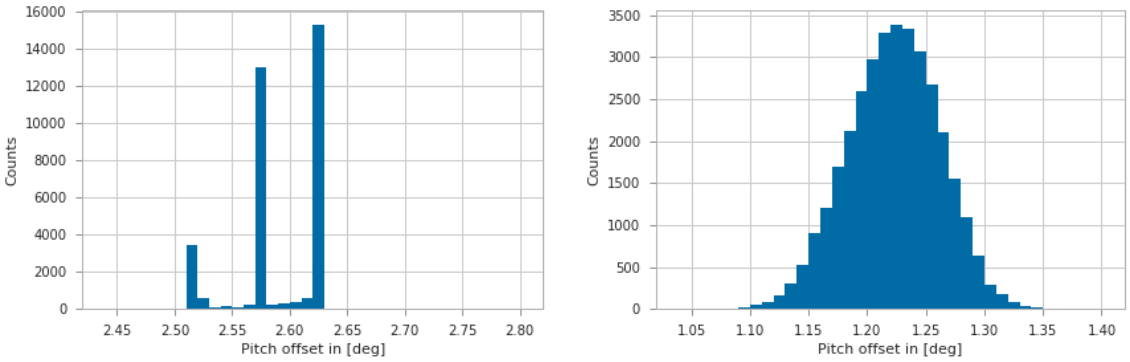

Figure 16: Distributions of the possible pitch offsets; DOM 2 left, DOM 14 right.

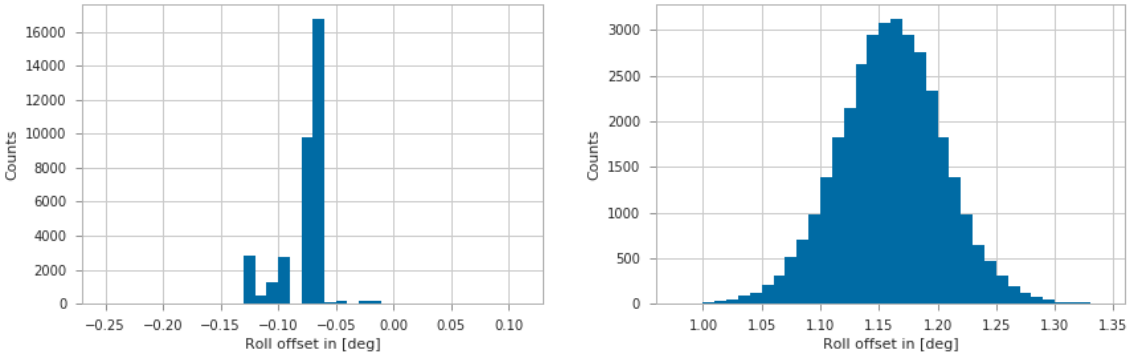

Figure 17: Distributions of the possible roll offsets; DOM 2 left, DOM 14 right.

For the lower DOMs (below DOM 11) the possible offsets are distributed similar to the left figures 16 and 17. Due to their lower height in the DU, the slopes $\frac{\mathrm{dr}}{\mathrm{dz}}$ of the positioning vectors of the DOMs are higher than the ones of the upper DOMs. This means that the signal to noise ratio for the lower DOMs is better than for the upper DOMs. Also, the possible offsets are distributed as sharp peaks for the most DOMs. From the set of possible offset will always the one be chosen, which is either the most common (highest bin) or, if there are more suitable peaks, the smallest offset in terms of value. This is due to the sea current, which is not perfectly at $v = 0\frac{\mathrm{cm}}{\mathrm{s}}$, allowing the DOMs to slightly tilt.

For the upper DOMs (above DOM 10) the signal to noise ratio is lower than that of the lower DOMs, but in difference to the lower DOMs, they seem less accurate (not DOM 12) as the distribution of possible offsets is a broad gauss distribution as seen in the right figures 16 and 17. This could be due to the fact that the DOMs are build at different locations with different testing facilities. For the calibration will therefore be the angle with the highest counts chosen.

5.5.3 Results

With the known offsets of each DOM for pitch and roll it should be possible to determine the correct line shape and sea current of the DU. A prime example is seen in figure 18.

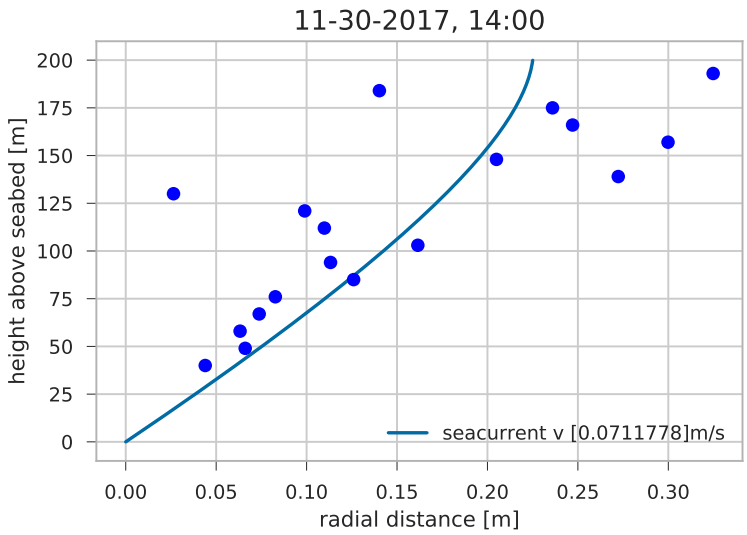

Figure 18: Line shape fit for all 18 DOMs after the calibration.

It quickly turns out that the calibration of the DOMs 9 to 18 is still not good enough as their calculated DOM positions are highly scattered as seen in figure 18. The reason for this is the low tilt of the DOMs in the upper part of the line, making them more vulnerable to small angle changes, which also includes the error of the offset. The broad distribution and therefore high standard deviation of the offsets for the highest DOMs makes a difference of several $\frac{\text{cm}}{\text{s}}$ in the determination of the sea current. For the first calibration will therefore only the first eight DOMs be used.
A calculation of the line shapes and sea current velocities over the time interval from 01.12.17 to 09.12.17 is made and will be compared with the ADCP data to control if the calibration via the offset determination is correct. This time span is chosen because of its large varieties of velocities.

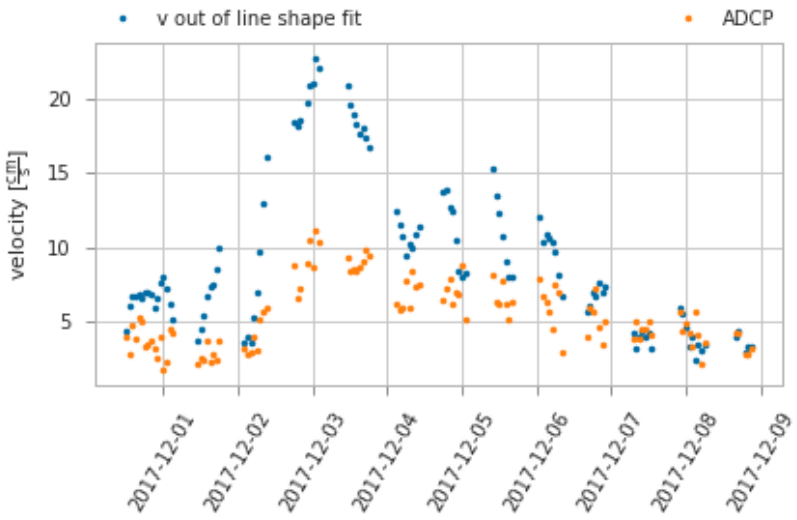

Figure 19: Time series of the velocities measured with the ADCP and the line shape model of ORCA.

As seen in figure 19, the from ORCA reconstructed velocity curve follows the trend of the velocity curve measured by the ADCP. But in contrast to the ADCP curve the ordinate of the ORCA curve distorted is. The distortion can be figured out by plotting a 2D histogram, where the two velocities are plotted against each other (figure 20). By the colour of a bin, it can be seen how often a certain ADCP and ORCA measured velocity appears at the same time.

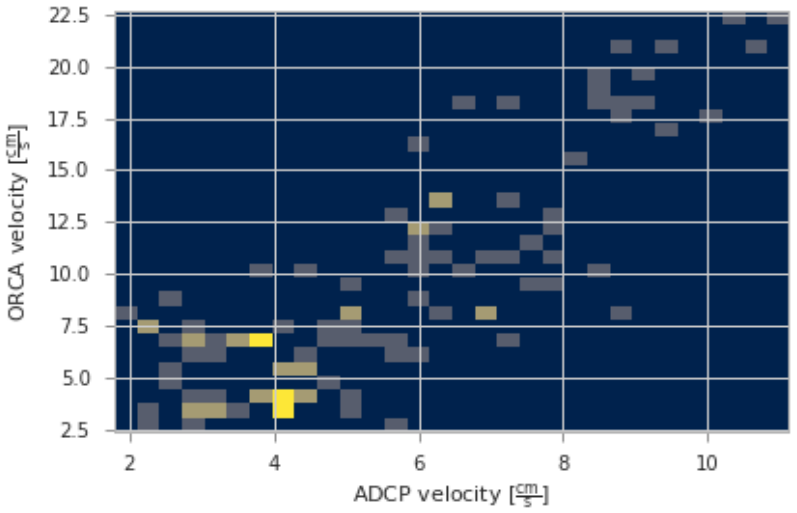

Figure 20: ADCP velocities plotted against the ORCA velocities.

The histogram can be divided into two main sections. The first section is where the ADCP velocity is below $5\frac{\text{cm}}{\text{s}}$ and the second one where it is above $5\frac{\text{cm}}{\text{s}}$. While the

ADCP velocity is below $5\frac{\text{cm}}{\text{s}}$, the ORCA velocity fluctuates around $5\frac{\text{cm}}{\text{s}}$. This is due to the calibration, which assumes a perfectly silent sea current. But this is obviously not the case. Therefore, the ORCA line shape model is unable to correctly measure sea currents below $5\frac{\text{cm}}{\text{s}}$.
The second section shows a linear relation between the from ADCP and ORCA measured velocities, which describes the ordinate distortion of the from ORCA measured velocities in the time series plot (figure 19). A divide of the calculated velocity through the slope of the straight gives the estimated velocity if it is above $5\frac{\text{cm}}{\text{s}}$ as seen in figure 21. The corrected velocity can then be used to calculate the real line shape with the line shape model.

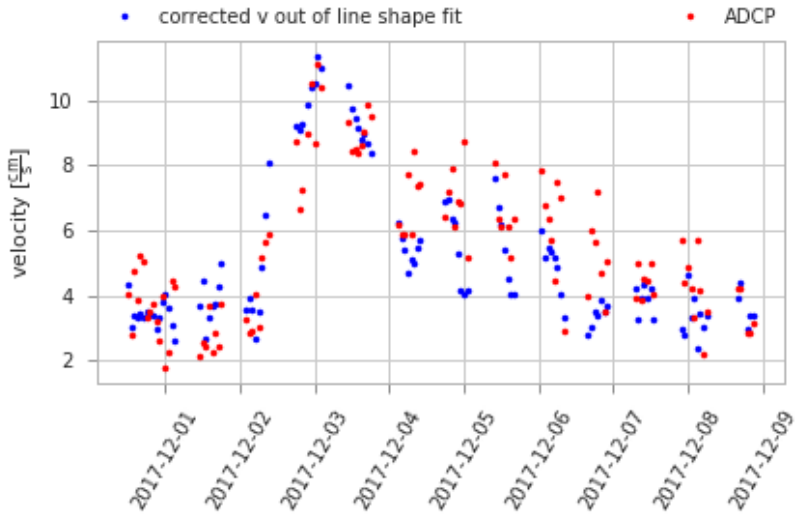

Figure 21: Corrected velocities with an correction factor of 2.

Looking at how the radial components of the DOM positions are calculated and the velocity is fitted,

$$r(z) = \left[\frac{b}{d} - \frac{ad - bc}{d^2} \ln\left(1 - \frac{d}{c} \cdot z\right)\right] v^2 \quad \text{, with} \quad v^2 = \frac{\mathrm{dr}}{\mathrm{dz}} \frac{c - dz}{a - bz} \ , \tag{25}$$

it is apparent that the only linear parameters, which could produce such behaviour, are a, b and the slope $\frac{\mathrm{dr}}{\mathrm{dz}}$. The rest of the parameters, c and d, have an additionally logarithmic term. Thus the flow resistance parameters or the slope and therefore the pitch and roll angles appear to be off. To create such linear distortion in velocity either the flow resistance parameters must be multiplied by a factor or the algorithm in the AHRS board to calculate the angles has a false factor multiplied. The uncertainty of the slope due to the uncertainty of pitch and roll could also contribute a constant offset of velocity, but this is not considered in the first recalibration.
A recalibration of the flow resistance parameters was tried by multiplicating different correction factor to them. But that did not lead to the expected solution as the ordinate distortion was still there (see figure 22). It could be possible that the ordinate distortion

is only linear in the first order and there is also a logarithmic term contributing to the wrong output. Therefore also the buoyancy parameters could be false.

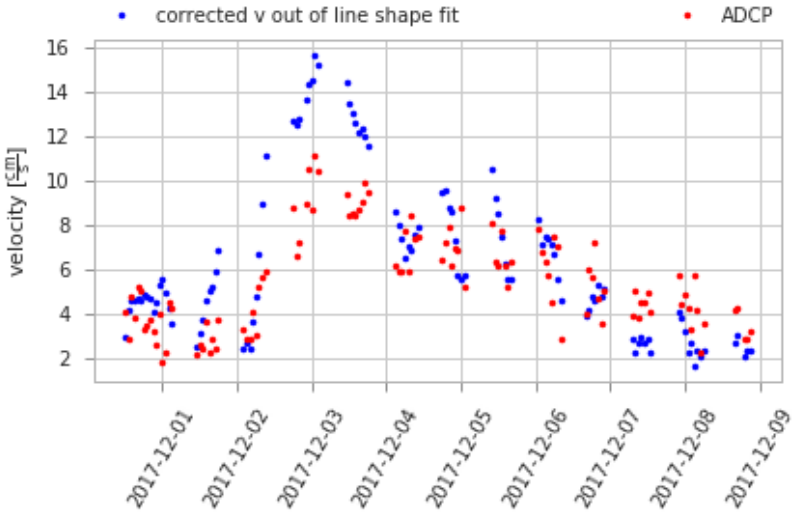

Figure 22: Corrected flow resistance parameters with an correction factor of 2.

To determine the direction of the current the positioning vector of each of the first eight DOMs can be projected onto the sea bed. By using the arctan2 function with the x and y components as argument, the angle relative to the x axis (east direction) can be measured. A addition of the yaw angle and correction of 270° to match the azimuth system should then lead to the direction angle. Even with the ±4° uncertainty of the yaw angle should a approximately direction determination be possible.
The first try at such a projection looks very promising (figure 23)

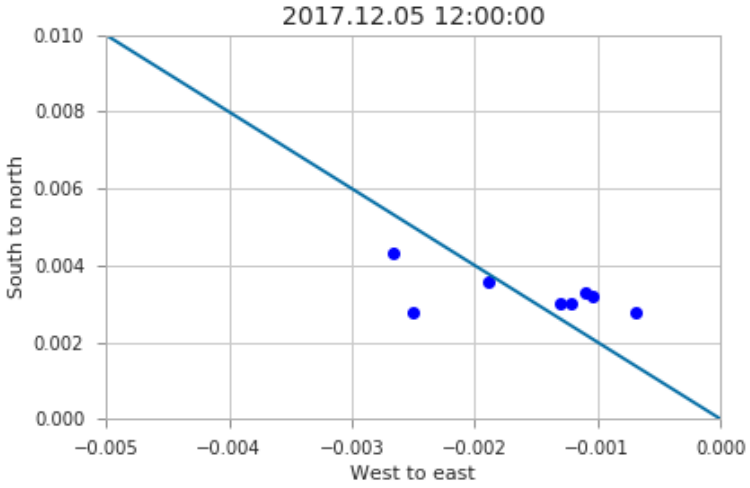

Figure 23: A line fit to demonstrate the alignment.

The points represent the heads of the positioning vectors of the DOMs, which got projected onto the sea bed. Therefore the plot has no units, because the positioning vectors are defined in a normalized space. The straight represents the DU and is also projected onto the sea bed. It will be fitted to match the points but has to go through the point of origin because the DU is anchored there. The slope of the straight is then the argument of the arctan2 function.
A detailed study was due to a lack of time not possible in this thesis.

6 Conclusion

It is definitely possible to use the ANTARES line shape model for the alignment of the ORCA detector, but the accuracy of determining the sea current and direction highly depends on the calibration of the Tait-Bryan angles of the DOMs. The first recalibration of the DOMs in this thesis is only the start and first try to make the data useable to determine the velocity and direction of the sea current. The moderate result of the recalibration is still only good enough for an online monitoring of the sea current strength, making the KM3NeT group independent of the data of the ADCP. But for a precisions measurement it is not good enough. Also will the direction determination with the represented recalibration only be an approximation as the yaw angle is still not calibrated. A simple option would be again a comparison with the ADCP data, where the difference between the angles is simply the offset. But further investigations are needed to evaluate if this method is accurate enough. All in all it should be possible in the future to produce convenient results as better calibrations in the laboratory or/and better calibration algorithms for the DOMs in the sea are developed.

Appendices

A Remaining AHRS time series

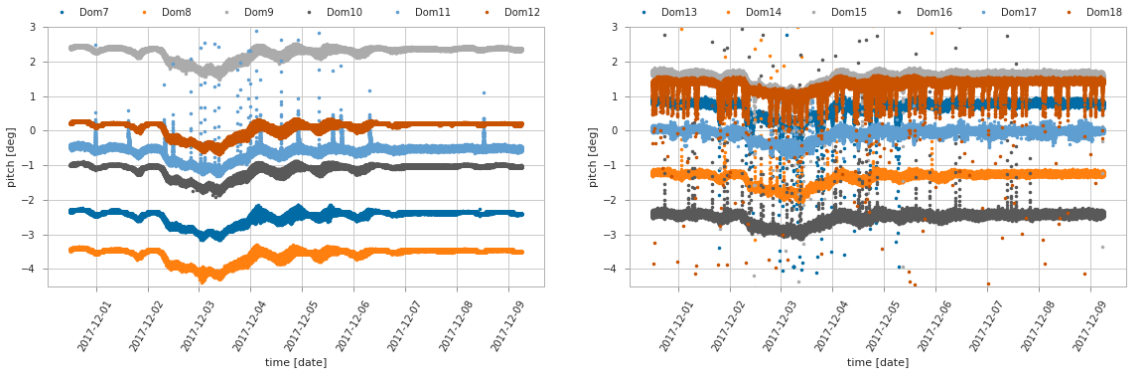

Figure 24: Pitch angle time series of the remaining DOMs.

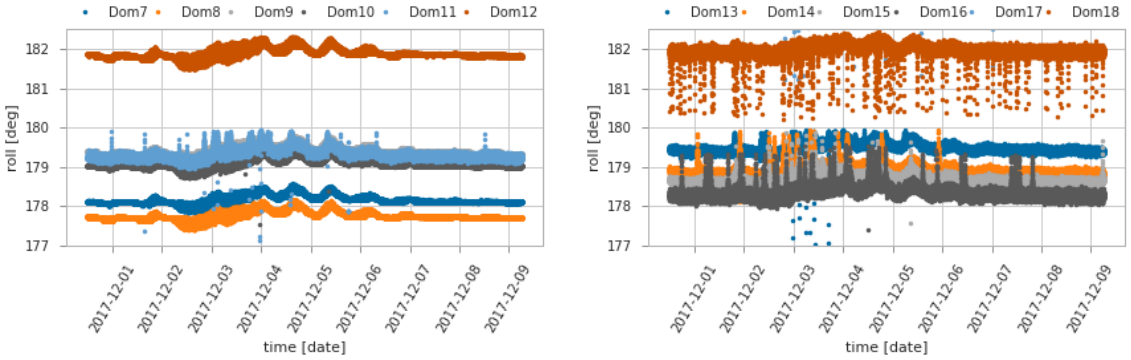

Figure 25: Roll angle time series of the remaining DOMs.

The high amplitudes in the time series of some plots are probable from malfunctions of the detectors as the duration of these are several minutes. Because of this long time span a possible collision with deep sea could animals excluded.

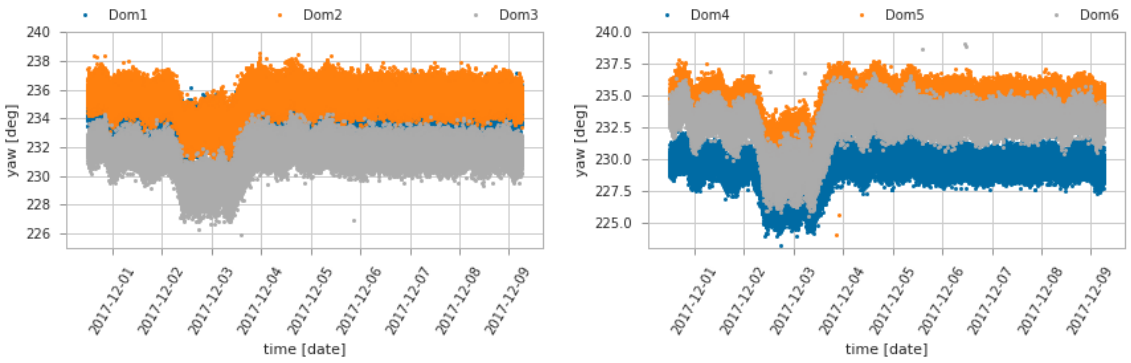

Figure 26: Yaw angle time series for DOM 1 to 6.

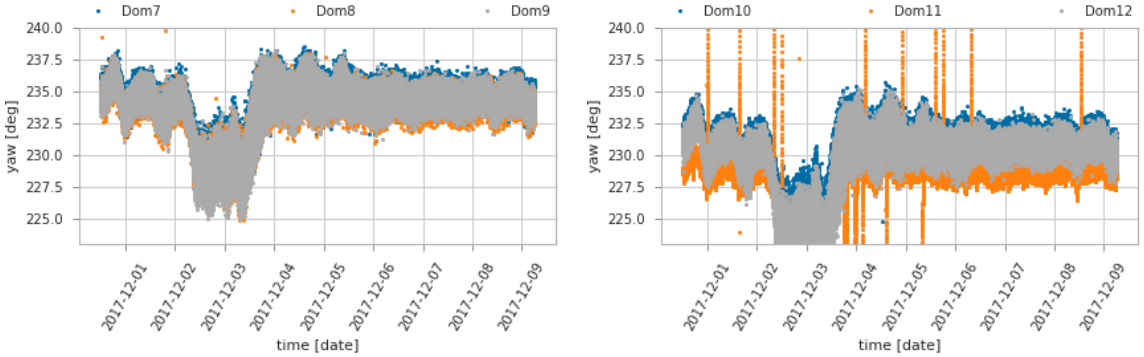

Figure 27: Yaw angle time series DOM 7 to 12.

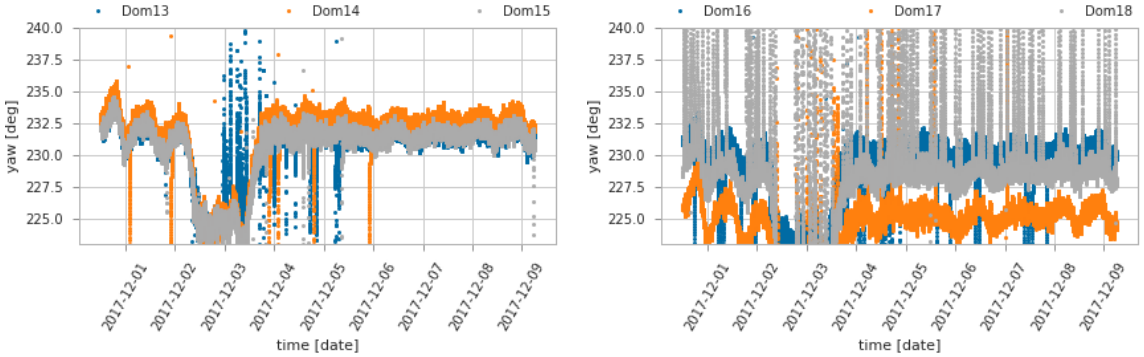

Figure 28: Yaw angle time series DOM 13 to 18.

B Remaining Offset distributions

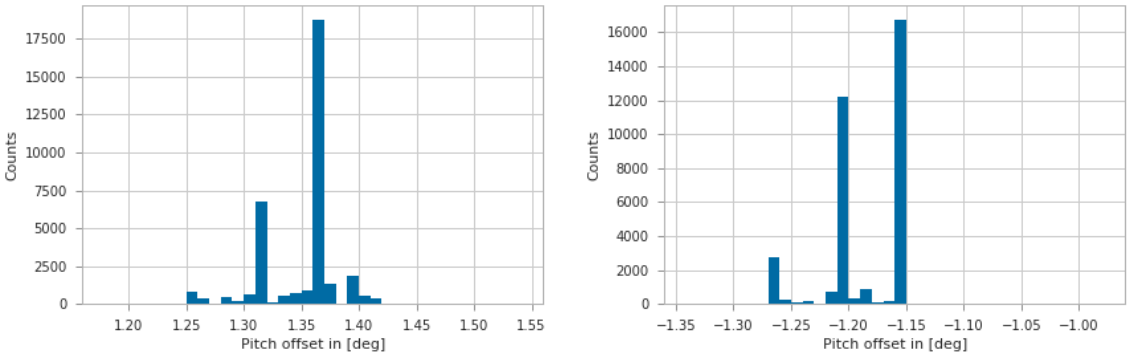

Figure 29: Pitch offsets; Left: DOM 1; Right: DOM 3.

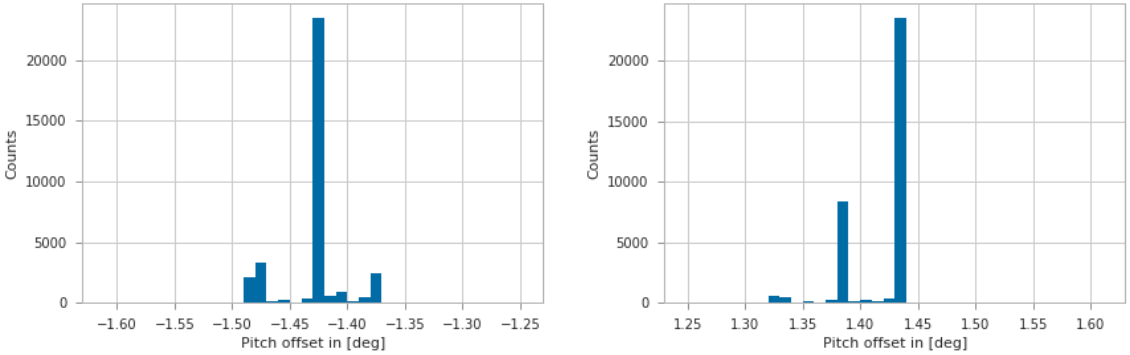

Figure 30: Pitch offsets; Left: DOM 4; Right: DOM 5.

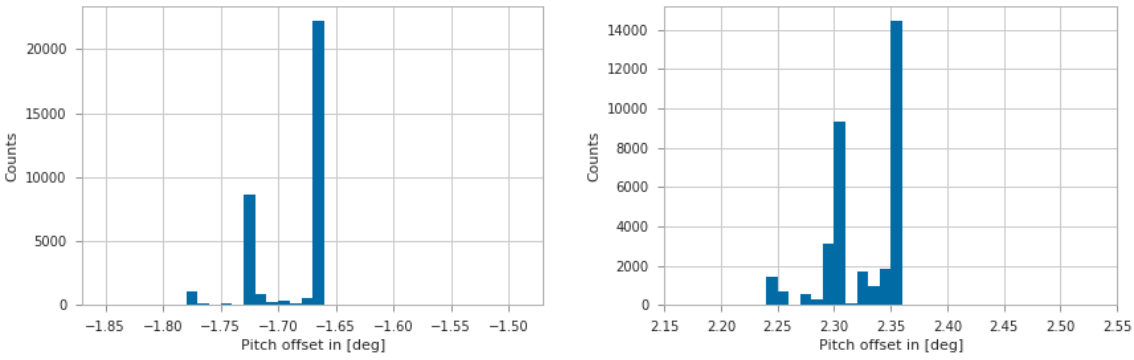

Figure 31: Pitch offsets; Left: DOM 6; Right: DOM 7.

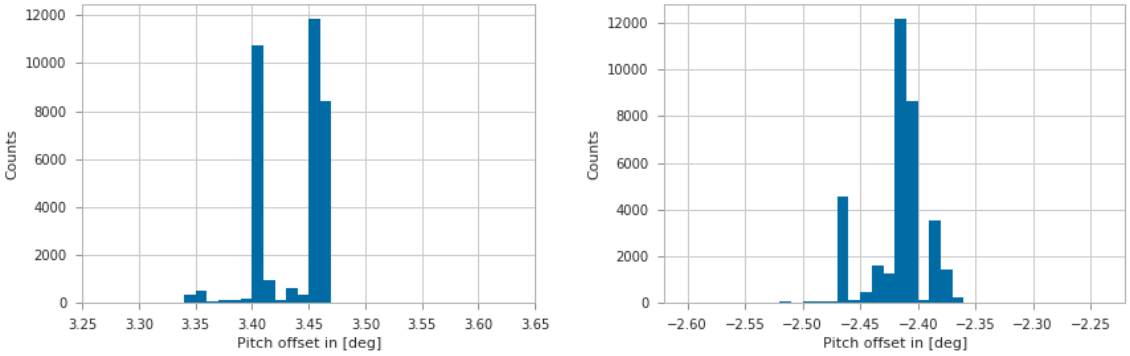

Figure 32: Pitch offsets; Left: DOM 8; Right: DOM 9.

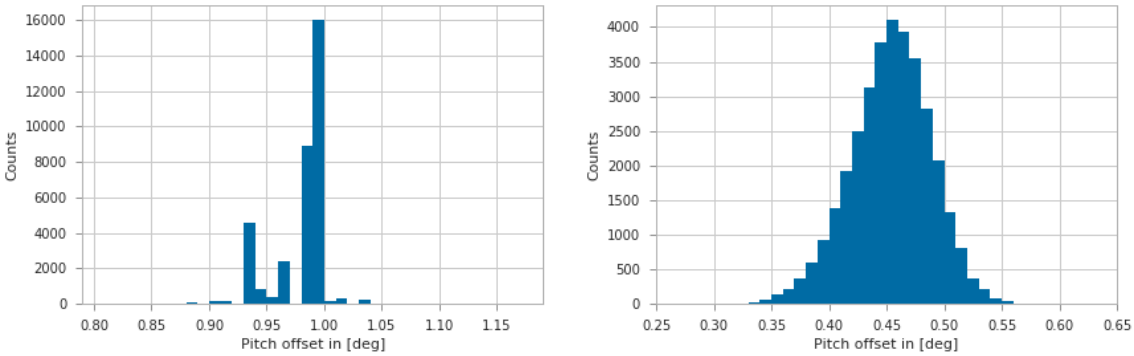

Figure 33: Pitch offsets; Left: DOM 10; Right: DOM 11.

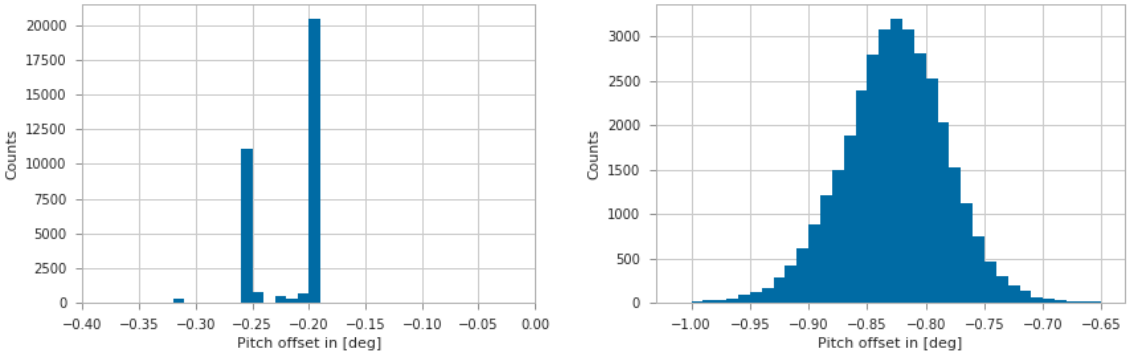

Figure 34: Pitch offsets; Left: DOM 12; Right: DOM 13.

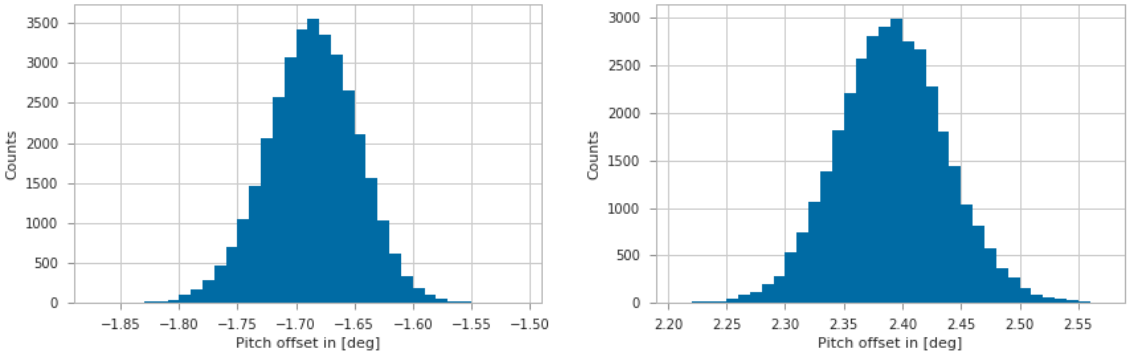

Figure 35: Pitch offsets; Left: DOM 15; Right: DOM 16.

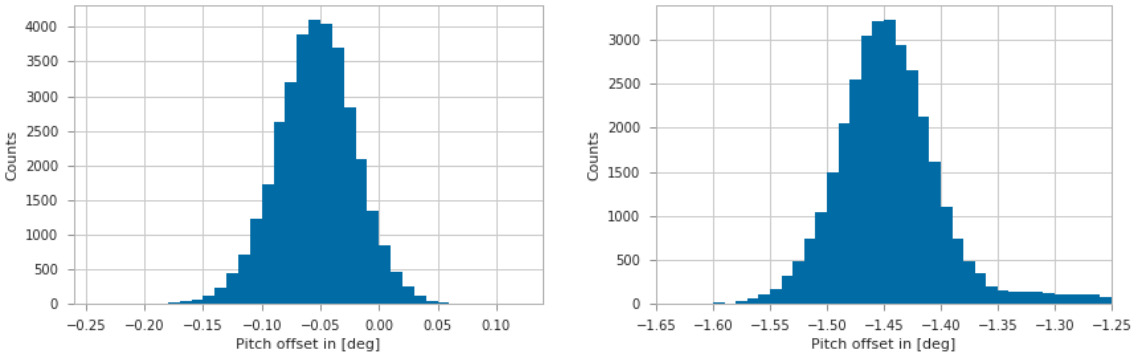

Figure 36: Pitch offsets; Left: DOM 17; Right: DOM 18.

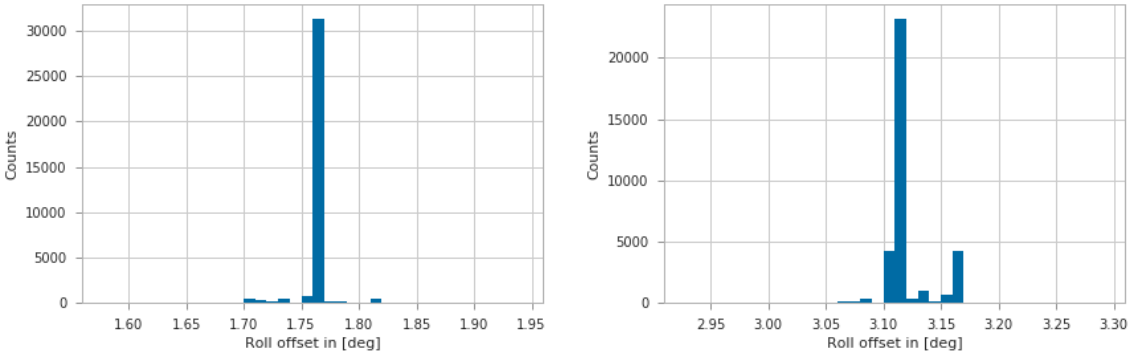

Figure 37: Roll offsets; Left: DOM 1; Right: DOM 3.

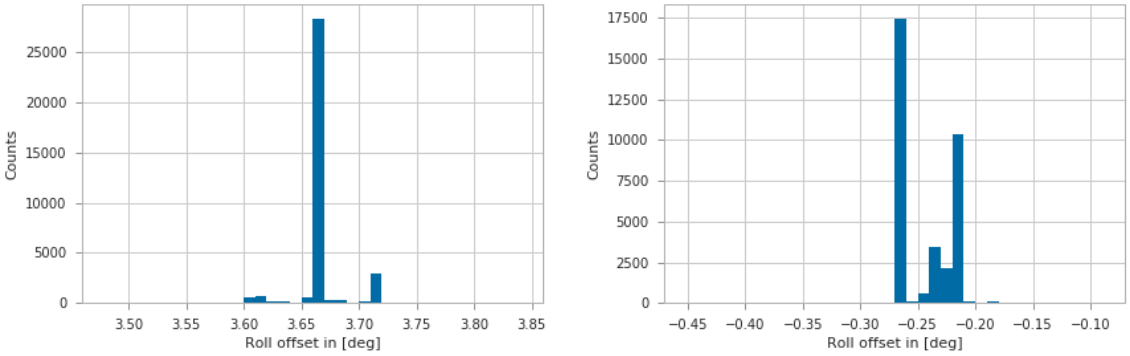

Figure 38: Roll offsets; Left: DOM 4; Right: DOM 5.

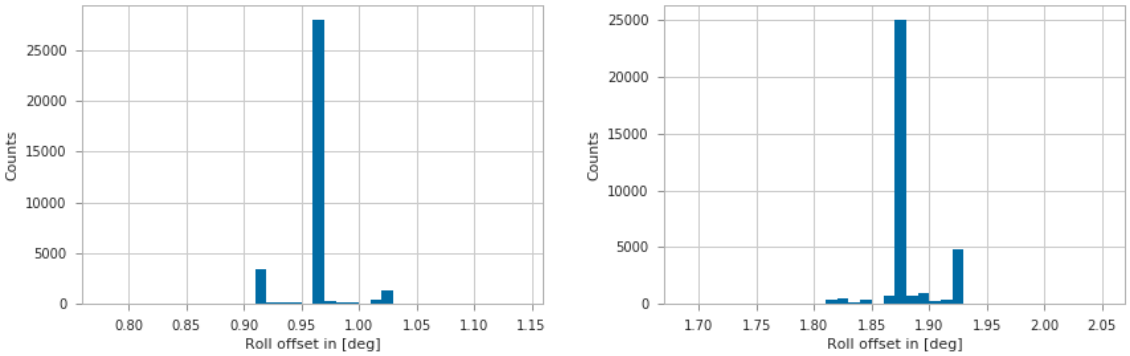

Figure 39: Roll offsets; Left: DOM 6; Right: DOM 7.

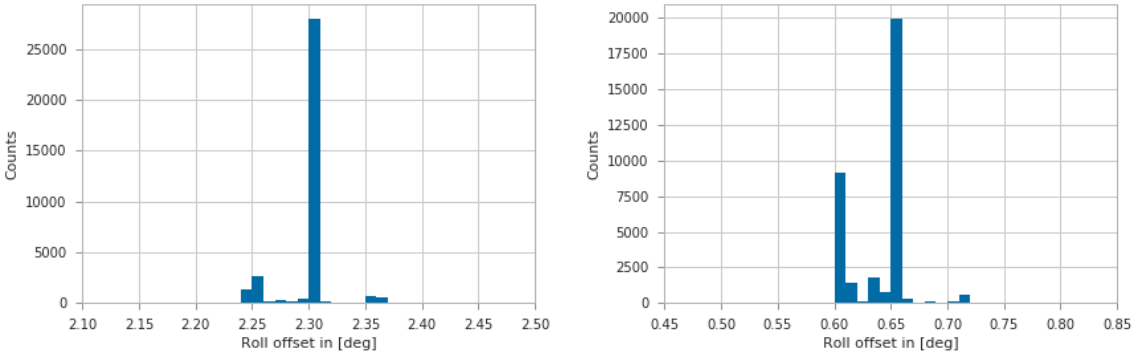

Figure 40: Roll offsets; Left: DOM 8; Right: DOM 9.

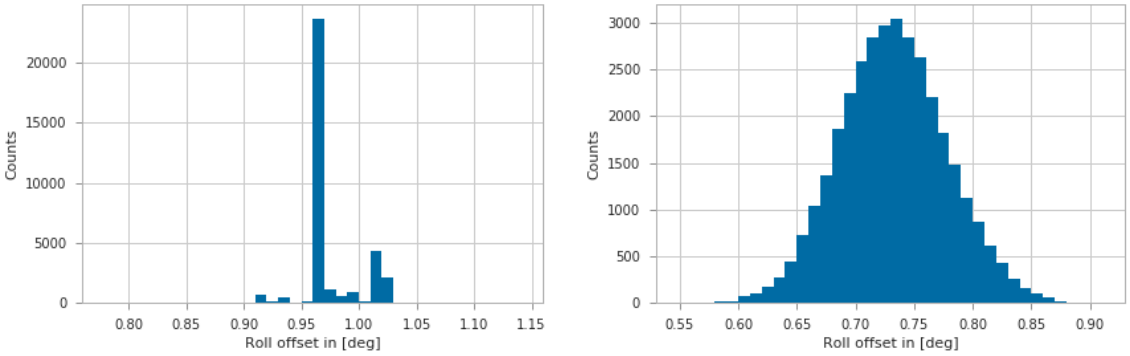

Figure 41: Roll offsets; Left: DOM 10; Right: DOM 11.

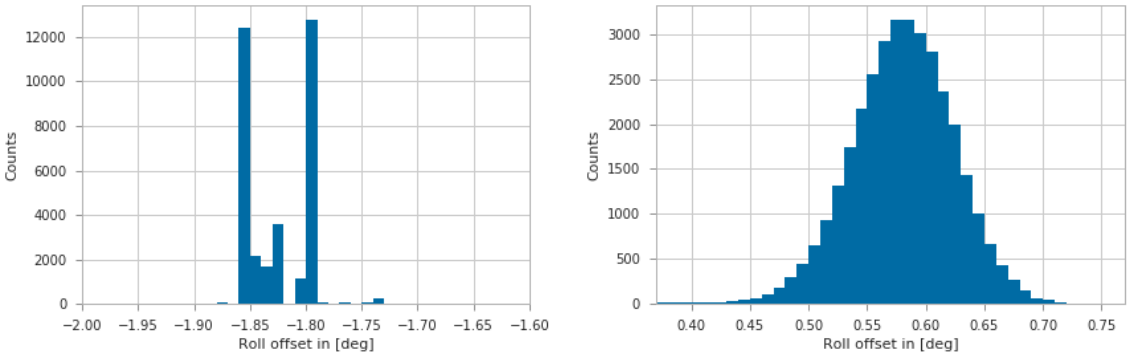

Figure 42: Roll offsets; Left: DOM 12; Right: DOM 13.

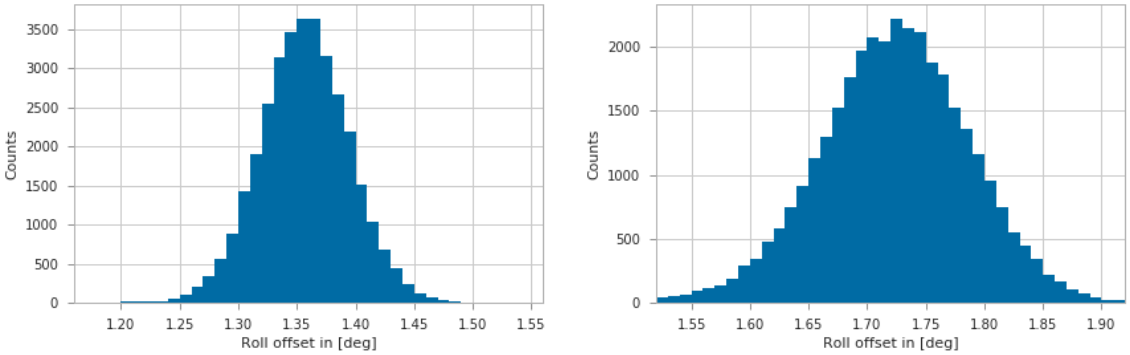

Figure 43: Roll offsets; Left: DOM 15; Right: DOM 16.

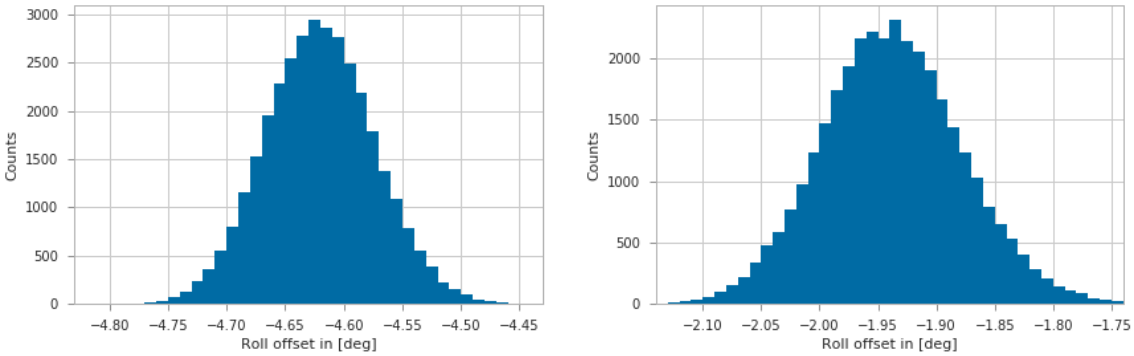

Figure 44: Roll offsets; Left: DOM 17; Right: DOM 18.

References

[1] Adrián-Martínez, S., Ageron, M., Aguilar, J., et al. 2012, JINST7 T08002

[2] Adrián-Martínez, S., Ageron, M., Aharonian, F., et al. 2016, Journal of Physics G: Nuclear and Particle Physics, 43 (8), 084001, 2016

[3] Biagi, S., Cresta, M., Hugon, C., et al. 2014-04-10, Internal paper: AHRS for CLBv2 documentation

[4] CASPER. 2017, Cherenkov Radiation, `https://casper.berkeley.edu/astrobaki/index.php/Cherenkov_Radiation`, accessed: 2018-07-16

[5] Dídac D.Tortosa, Juan A. Martínez-Mora, M. A. 2018-05-08, DU line fit analysis

[6] Dr. Dominique Lefevre. 2018, Internal communication

[7] Dr. Thomas Eberl. 2018, Internal communication

[8] Nobelprize.org. Nobel Media AB 2014. Web. 31 Jul 2018, The Nobel Prize in Physics 2015 - Scientific Background: Neutrino Oscillations, `http://www.nobelprize.org/nobel_prizes/physics/laureates/2015/advanced.html`, nobel Media AB 2014. Web.

[9] Nortek. 2018, Aquadopp 3000 m, `https://www.nortekgroup.com/export/pdf/Aquadopp%203000%20m.pdf`, accessed: 2018-08-08

[10] Patrignani, C. et al. 2016, Chin. Phys., C40, 100001

[11] Rose, D. 2015, Rotations in Three-Dimensions: Euler Angles and Rotation Matrices, `http://danceswithcode.net/engineeringnotes/index.html`, accessed: 2018-07-25

[12] S. Biagi, K. Melis, M. L. August, 2018, Measurement of the muon rate dependence on the sea depth with the KM3NeT neutrino telescope

[13] Schmitz, N. 1997, Neutrinophysik (Stuttgart: Teubner-Studienbücher: Physik)

[14] Woods Hole Oceanogrpahic Institution. 2018, Acoustic Doppler Current Profiler (ADCP), `http://www.whoi.edu/page.do?pid=8415&tid=7342&cid=819`, accessed: 2018-08-02

Statement of Authorship

I hereby certify that this thesis has been composed by me and is based on my own work, unless stated otherwise. No other persons work has been used without due acknowledgement in this thesis. All references and verbatim extracts have been quoted, and all sources of information, including graphs and data sets, have been specifically acknowledged.

Place, date

Signature

Acknowledgements

I would like to thank everyone who has supported me during my bachelor thesis. Special thanks to:

- My fiancée Stefanie Vogl for her never ending support and cheering me up
- Dr. Thomas Eberl and Dr. Jannik Hofestädt for the countless advices and being the best supervisors I could imagine
- Steffen Hallmann and again Dr. Thomas Eberl for letting me take part of the ANTARES shift
- Sebastian Konrad and Johann Brand for the pleasant working atmosphere and tipps and tricks
- My mother, because I would not be standing here without her